



Effect of Zn content on microstructure evolution in Al–Zn alloys processed by high-pressure torsion

Anwar Q. Ahmed^{1,2}, Dávid Ugi¹, János Lendvai¹, Maxim Yu. Murashkin^{3,4}, Elena V. Bobruk³, Ruslan Z. Valiev^{3,4}, Nguyen Q. Chinh^{1,a)} 

¹Department of Materials Physics, Eötvös Loránd University, Pázmány Péter Sétány 1/A, Budapest 1117, Hungary

²College of Science, University of Kufa, Najaf 54001, Iraq

³Institute of Physics of Advanced Materials, Ufa University of Science and Technology, 32 Z. Validi St., Ufa 450076, Russia

⁴Laboratory for Dynamics and Extreme Performance of Advanced Nanostructured Materials, Saint Petersburg State University, 7-9 Universitetskaya Nab., St. Petersburg 199034, Russia

^{a)}Address all correspondence to this author. e-mail: chnh@metal.elte.hu

Received: 7 October 2022; accepted: 6 June 2023; published online: 30 June 2023

Al–Zn alloys having different Zn contents of 2, 5, 10 and 30 wt% were processed by high-pressure torsion (HPT) to produce ultrafine-grained (UFG) materials. Microstructural features of these UFG Al–Zn alloys were investigated using depth-sensing indentations, focused ion beam (FIB), scanning electron microscopy (SEM) and differential scanning calorimetry (DSC). Emphasis was placed on the microstructure evolution of the alloys with different Zn-concentration which demonstrated substantially different mechanical behavior, exhibiting superductility with increasing Zn content. It was shown that in every case, HPT resulted decomposition in the microstructure, but there is a significant difference between the microstructures of alloys with low and high Zn content. Based on the microstructural observations, a scenario is proposed about that how the decomposed microstructure developed during HPT process in low- and high Zn-containing Al–Zn alloys, influencing their mechanical behavior.

Introduction

Being one of the basic materials in the Al industry, alloys of the Al–Zn system always retain attractiveness in material research. Both special compositions, such as eutectic and eutectoid, and solid solution Al–Zn alloys have been extensively studied [1–11]. During the past two decades, several studies were devoted to grain boundary phenomena of these alloys [3, 6–8, 12–17], since it is well known that the mechanical properties of an alloy of given composition are strongly influenced by the grain size and eventually by grain boundary segregation and/or the formation of a grain boundary phase. In order to achieve extreme grain-refinement in bulk Al–Zn samples most commonly severe plastic deformation (SPD) is applied [18]. Previous works [3, 7, 9, 16, 17] have shown some unexpected results on the behaviors of Al–Zn alloys processed by severe plastic deformation (SPD) using the high-pressure torsion (HPT) technique [19]. Microstructure of the HPT-processed Al–Zn alloys was carefully studied using transmission electron microscopy (TEM). Together with the grain-refining effect, HPT processing has also resulted in significant decomposition of the solid solution state in the

alloys having high Zn contents. The experimental observations of the HPT-processed microstructure [3, 5–8] have shown the formation of Zn particles, in the Al/Al grain boundaries and mainly in grain boundary triple junctions and also inside the Al grains. Furthermore, high resolution electron microscopy (HRTEM) and energy-dispersive X-ray spectroscopy (EDS) investigations [5, 6, 14–17] have revealed thin Zn-rich layers in grain boundaries of the SPD processed UFG Al–Zn alloys having Zn content higher than 10 wt%. These UFG alloys show intensive grain boundary sliding (GBS) during plastic deformation, even at room temperature [3–5, 16, 17]. It has been shown that the intensive GBS in the system having Zn-wetted grain boundaries is controlled by relatively high diffusion of Zn atoms along grain boundary [16, 17]. In addition, these materials showed an unexpected softening despite the UFG microstructure [5, 20, 21].

It should be noted that significantly increasing the Zn content to 50 weight percent (in Al-30 at.% Zn alloy) [16], the effect of the wetted grain boundaries becomes more pronounced in the HPT-processed sample, leading to high strain rate sensitivity of

0.4 and superplasticity over 400% tensile elongation at room temperature. However, the strong Zn-wetted grain boundaries in this extra concentrated sample have enhanced grain boundary energy, reducing the stability of grain boundaries. Because of this, the HPT-processed microstructure suffered recovery during storage at room temperature. The average grain size has significantly increased from 280 to 550 nm during room temperature superplastic deformation [16].

The objective of the present study was to reveal the correlation between Zn concentrations and the microstructural and mechanical properties of Al–Zn alloys processed by HPT, giving thereby further details on the dependence of mechanical properties on the grain and precipitate microstructure of UFG Al–Zn alloys.

Experimental results and discussion

Mechanical properties of HPT-processed Al–Zn alloys

Mechanical tensile tests to reveal the superplastic features during the deformation of the UFG Al–Zn alloys were performed at room temperature in a strain rate range of 10^{-2} to 10^{-4} s^{-1} in accordance with [6, 21]. Characterization of the mechanical properties at room temperature demonstrated a direct dependence of the ultimate tensile strength (UTS) on the Zn content increase in the binary Al–Zn alloys (for Al–2Zn, $\sigma = 116\text{--}122 \text{ MPa}$; for Al–5Zn, $\sigma = 198\text{--}220 \text{ MPa}$; for Al–10Zn, $\sigma = 290\text{--}300 \text{ MPa}$; for Al–30Zn, $\sigma = 280\text{--}320 \text{ MPa}$), the ductility of all the alloys was 30–40% in the whole strain rate range. A different behavior was revealed in Al–30Zn sample deformed at a strain rate of 10^{-4} s^{-1} , where the flow stress decreased to $\sigma = 123 \pm 3 \text{ MPa}$, the ductility reached 235% and the strain rate sensitivity parameter was $m = 0.36$ [6, 21].

Figure 1 shows the hardness of the Al–Zn samples before (as annealed) and after HPT processing in the function of Zn concentration. Considering the effect of the alloying atoms, it can be seen that the Vickers hardness, HV of the coarse-grained annealed samples is “normally” increasing linearly with the increasing Zn content (see the black square symbols in Fig. 1). In theory, if the microstructure had remained in solid solution during the HPT process, taking into account also the strengthening role of Hall–Petch effect for pure Al [22] beside this “normal” solute-strengthening, the hardness of the Al–10Zn sample (with average grain size of 435 nm) and of the Al–30Zn sample (with average grain size of 350 nm) would be about 90 and 160, respectively (see blue half-right circle symbols). Instead, however, experimental results show much lower hardness for the two high Zn-containing alloys, indicating a softening in these HPT-processed alloys. The hardness of the HPT-processed alloys become almost constant at the value of 72 for Zn concentration higher than 5% (see red

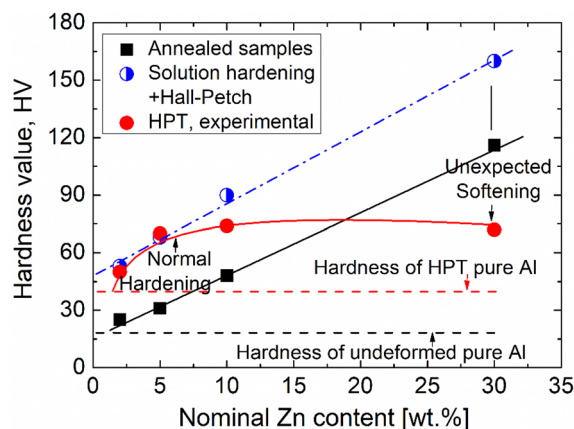


Figure 1: Effect of HPT processing on microhardness in the function of the nominal Zn content.

circle symbols). The softening of the high Zn-concentrated alloys is also the consequence of the decomposition of the initial supersaturated microstructure [5, 16, 17, 20] during severe plastic deformation, which leads to a decrease in the concentration of solute Zn in the Al matrix and thus to a drop in hardness. Taking into account the solubility of about 2wt% at room temperature for Zn in Al, the decomposition in the low Zn-content (Al–2Zn and Al–5Zn alloys) is not significant so that normal hardening—due to the Hall–Petch effect—is still observed (see in Fig. 1).

It should be emphasized that the decomposition during SPD resulted not only the formation of Zn particles, but also the segregation of Zn atoms into Al/Al grain boundaries, which was recently interpreted by simulation calculations [23]. Because of significant segregation, more than 50% of the Al/Al grain boundaries in the HPT-processed Al–30Zn alloy is wetted by Zn-rich layers [5, 7], by which this alloy can show unique plastic behaviors. Figure 2 shows the stress–strain ($\sigma - \varepsilon$) curves obtained by compressing micro-pillars of the HPT-processed Al–30Zn sample at room temperature at different strain rates. It can be seen that the flow stress is strongly dependent on the strain rate, leading to a high strain rate sensitivity (SRS) of about 0.36, similarly to that obtained by tensile test. It is well known that ultrafine-grained materials generally exhibit low SRS of about 0.01–0.03 [24]. The high SRS of the HPT-processed Al–30Zn sample is accompanied with its room temperature superductility for an elongation of 235% [6, 21], which is also an unexpected phenomenon in the case of UFG.

The unexpectedly high SRS, as well as the unexpected superductility are the consequence of the high fraction of grain boundaries wetted by Zn layers, which greatly facilitate the grain boundary sliding (GBS) mechanism [3, 5]. Figure 3 shows SEM micrographs of the surface morphology of micro-pillar deformed at pressing velocity of 10 nm/s (denoted by

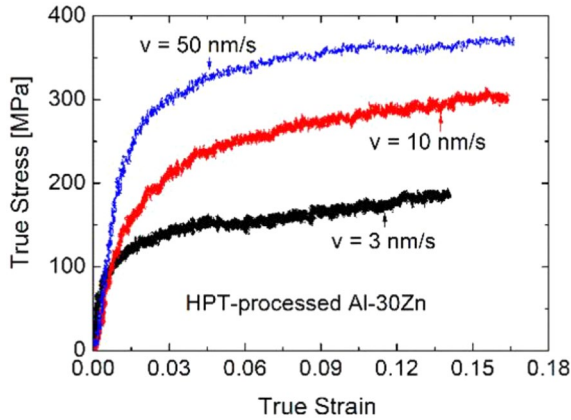


Figure 2: Stress–strain curves obtained by compressing micro-pillars at room temperature, at different pressing velocities on the surface of HPT-processed Al-30Zn sample.

red curve) shown in Fig. 2. demonstrating clearly the occurrence of intensive GBS during plastic deformation at room temperature.

Because of intensive GBS, the displacement of the fine grains relative to each other can be clearly observed in the higher magnification image of Fig. 3(b), where ultrafine grains emerging from the surface are visible as rings around the pillar-sample.

Characterization of microstructure by DSC investigations

Dissolution of precipitates in HPT-processed Al–Zn alloys and characteristic specific enthalpy

Figure 4 shows typical DSC thermograms taken on the investigated samples. The curves obtained at the same heating rate, V of 30 K/min on HPT-processed alloys containing 2, 5, 10 and 30wt% Zn can be seen in Fig. 4(a), and those for HPT-processed Al-5Zn alloy at different heating rates are shown in Fig. 4(b). In all cases only an endothermic process can be observed on the thermograms, indicating the dissolution of Zn precipitates. Furthermore, the specific enthalpy of dissolution, ΔH ,—the area belonging to the peak when plotting the

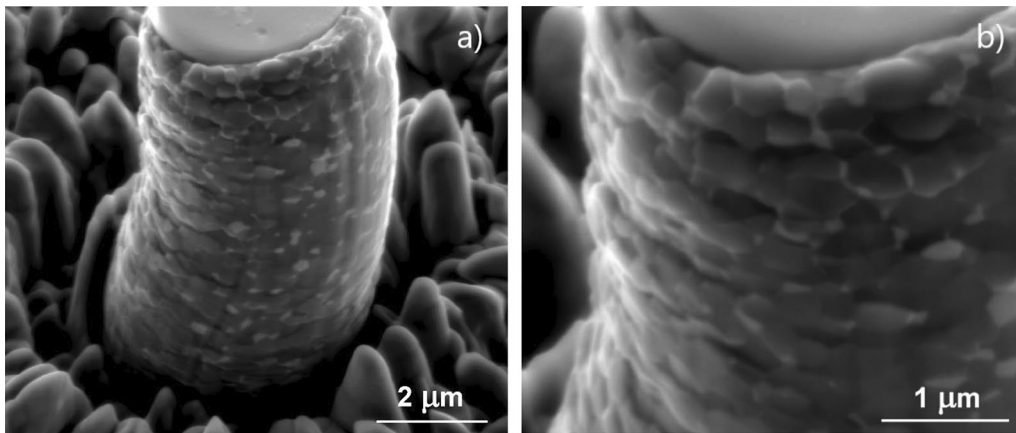


Figure 3: Surface morphologies of compressed micro-pillars for the HPT Al-30Zn sample in (a) low and (b) high magnifications.

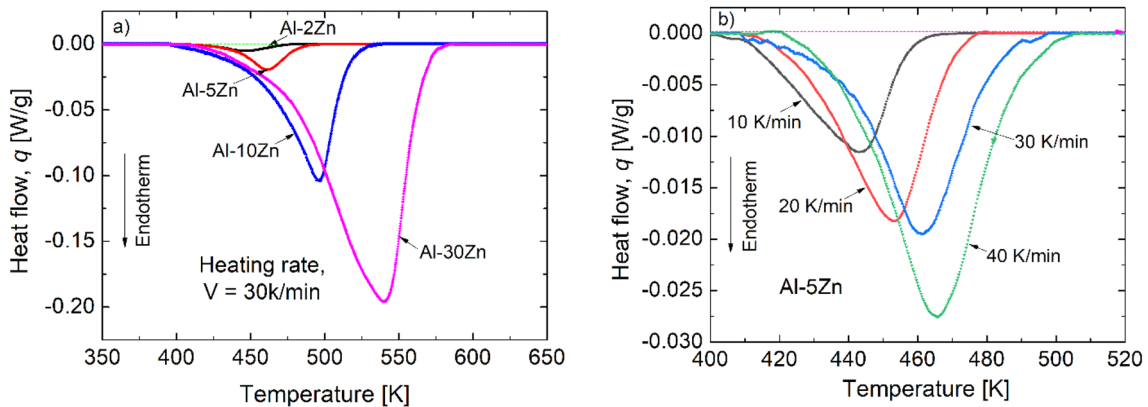


Figure 4: Typical DSC thermograms taken (a) on HPT-processed alloys containing 2, 5, 10 and 30wt% Zn at 30 K/min heating rate, and (b) on HPT-processed Al-5Zn at different heating rates.

heat flow in the function of time—is unambiguously increasing with increasing Zn-content [Fig. 4(a)].

Figure 5 shows the specific heats of dissolution, ΔH as a function of the heating rates for the different concentration alloys [Fig. 5(a)] as well as the function of Zn concentration [Fig. 5(b)]. It can be seen that the value of ΔH is independent of the heating rate at a given Zn concentration [see Fig. 5(a)], but it is linearly increasing with the Zn content of the sample [Fig. 5(b)]. It is clear that the magnitude of the ΔH is related to the amount of Zn precipitates/mass unit formed in the given alloy in the decomposition taking place during the HPT process. Previously reported results [7, 25] have shown that, due to decomposition, almost only the amount of Zn corresponding to the equilibrium solubility at room temperature (somewhat below 2%) remains in solid solution. Therefore, the linear relationship shown in Fig. 5(b) is a completely normal, expected connection. The value of ΔH obtained for the Al-2Zn alloy is negligible and it increases linearly with the Zn content of the alloys.

Results of the DSC measurements also show that at a given Zn concentration, the peak-temperature of the endothermic peak is shifted to higher temperatures with increasing heating rates [see Fig. 4(b)], indicating that the dissolution is a thermally activated – time dependent process. The maximum heat flow takes place at higher temperature in faster process when applying higher heating rate. In order to examine the dissolution process, Avrami-Johnson-Mehl theory [26] is incorporated and addressed to determine kinetics parameters, such as the dissolved volume fraction, Y and the rate of transformation, dY/dt , as well as the activation energy, Q_{ac} for the dissolution process.

Kinetic parameters for dissolution reactions

In general, the progress of reaction over a wide range of temperatures in DSC run of non-isothermal transformations shows the developing of kinetics of precipitations and dissolution of precipitates, where the total heat effects $Q(T)$ detectable between

the initial temperature, T_i of a peak and temperature, T can be given by:

$$Q(T) = \frac{EA(T)}{mV} \quad (1)$$

where m and V represent the mass of the sample and heating rate, respectively. E is a calibration constant [27]. $A(T)$ characterizes the area under the peak in the range of temperatures extended from T_i to T , obtained by integrating the heat flow, q by temperature:

$$A(T) = \int_{T_i}^T qdT. \quad (2)$$

It should be noted that in the present case, the heat flow, q and then $A(T)$ and $Q(T)$ are all characterizing dissolution reactions. If T_f represents the ultimate temperature of the peak,

$$Q(T_f) = \frac{EA(T_f)}{mV} \quad (3)$$

Assuming that Q_0 is the heat effect per mole of precipitate, therefore, the total heat effects can be expressed as

$$Q(T) = Q_0 \cdot n(T) \quad (4)$$

And

$$Q(T_f) = Q_0 \cdot n(T_f), \quad (5)$$

where $n(T)$ represents the number of moles for the precipitate that dissolve per unit mass of material up to temperature, T during DSC.

Combining Eqs. (1), (3) and (4), the volume fraction,

$$Y(T) = \frac{n(T)}{n(T_f)}$$

of the dissolved precipitates can also be given by

$$Y(T) = \frac{A(T)}{A(T_f)}, \quad (6)$$

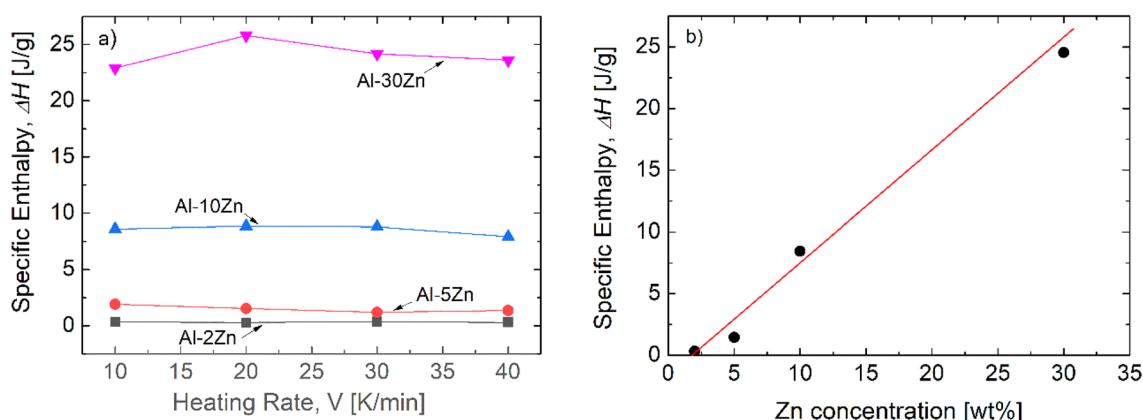


Figure 5: Specific enthalpy, ΔH , (a) obtained from the DSC thermograms taken at different heating rates and (b) in the function of Zn concentration.

which can be then determined by applying Eq. (2) for DSC thermograms.

Figure 6 shows the experimentally determined Y - T plots characterizing the dissolution at different heating rate for the investigated Al-Zn alloys.

It can be seen that the Y - T curves are characterized typically with a sigmoidal shape and shifted to higher temperature as the heating rate and solute concentration are increased, similarly to the heat flow vs temperature (q - T) relations. In this work, the kinetics of alloys with low and high Zn content show a significant change. It can be seen, for instance, that the dissolution process is achieved at 458 and 552 K for Al-2Zn and Al-30Zn alloys, respectively, when applying the heating rate of 10 K/min under the same conditions. These final temperatures are shifted to 480 and 580 K for Al-2Zn and Al-30Zn, respectively in the case of higher heating rate of 40 K/min [see Figs. 6(a) and (d)]. This difference is certainly related to the decomposed microstructures of the HPT-processed alloys. The transmission electron microscopy (TEM) images of Fig. 7 demonstrate a clearly visible difference between the two mentioned alloys.

In case of low Zn content (Al-2Zn), the supersaturated solid solution typically decomposes into Guinier–preston (GP) zones and followed by a few density number of semi-coherent metastable phase nucleated inside grains through HPT process. Likewise, it was impossible to detect a significant Zn segregation along GB and triple junction due to the Zn concentration lack. As a result, for this phenomenon, microstructure has a relatively high average grain size of about 1 μm , because lacking of pinning effect [Fig. 7(a)].

For the high Zn concentration (Al-30Zn), the supersaturated solid solution decomposed by discontinuous precipitation (DP) mechanism. This decomposition process of yields two products in form of a lamellar of (Al) and (Zn) phases which aggregated behind a migrating reaction front along which Zn atoms have the ability to redistributed easily. Therefore, the kinetic of reaction is determined by the velocity of this migrating reaction front. A large volume fraction of Zn particles has nucleated and growth along GBs and triple junctions in alloys having high Zn content (Al-10Zn and Al-30Zn) [7]. This kind of segregation enhance the pinning effect, which in turn drives the decomposition process to produce a smaller grain at higher

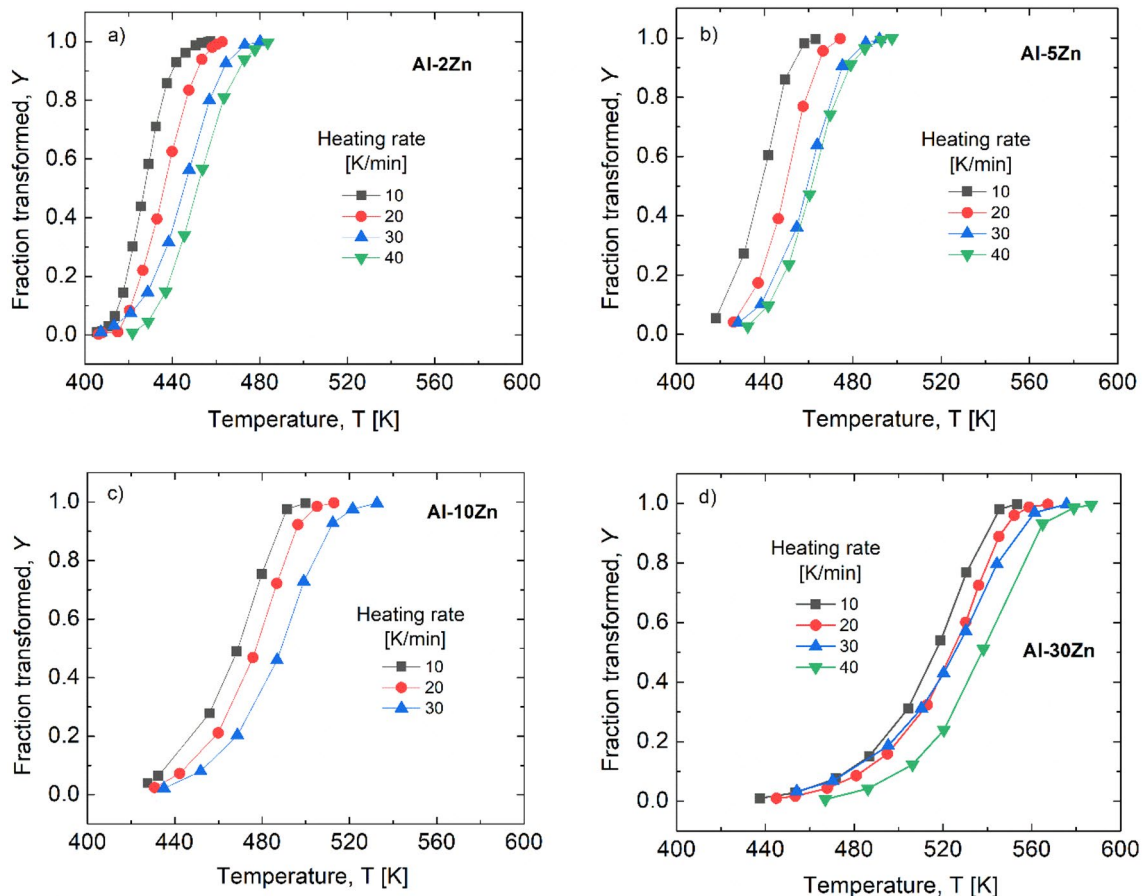


Figure 6: Plots of Y - T characterizing dissolutions at different heating rates for (a) Al-2Zn, (b) Al-5Zn, (c) Al-10Zn and (d) Al-30Zn alloys.

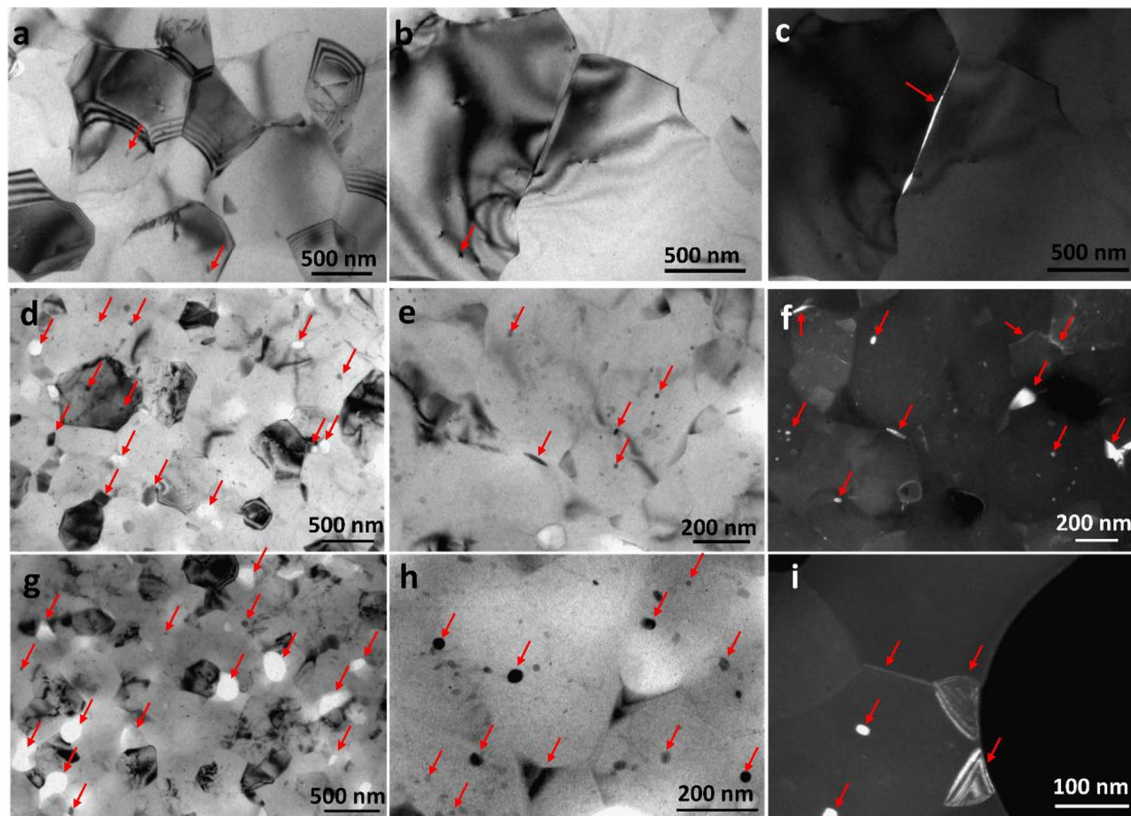


Figure 7: TEM images of the HPT-processed Al-Zn alloys, showing the ultrafine-grained (UFG) structure and Zn particles at triple junctions and in the grain interiors, Zn interlayers at the Al grain boundaries: (a, b) bright-field images of the Al-2Zn alloy; (c) dark-field image of the Al-2Zn alloy; (d, e) bright-field images of the Al-10Zn alloy; (f) dark-field image of the Al-10Zn alloy; (g, h) bright-field images of the Al-30Zn alloy; (i) dark-field image of the Al-30Zn alloy. (Some Zn particles are shown by small red arrows).

temperature. Therefore, the average grain size of high Zn-concentrated HPT-processed samples is lower than 500 nm. Furthermore, intragranular nanoscaled Zn particles of low and high densities can also be observed, as shown in Fig. 7.

In the knowledge of the fraction volume, $Y(T)$, the rate of transformation, dY/dt can also be experimentally calculated using the heating rate, V as following:

$$\frac{dY}{dt} = \frac{dY}{dT} \cdot \frac{dT}{dt}, \quad (7)$$

or

$$\frac{dY}{dt} = \frac{dY}{dT} \cdot V \quad (8)$$

Figure 8 shows the rate of transformation, dY/dt in the function of temperature, T at different heating rate for the investigated Al-Zn alloys. It is clear that each $dY/dt - T$ curve has a maximum, which is also shifted to higher temperature as the heating rate and solute concentration are increased, similarly to the heat flow vs temperature ($q-T$) relations (in Fig. 4) and the above mentioned $Y-T$ curves (in Fig. 6). It can be seen that the peak of the maximum rate of transformation is shifted from

427 to 454 K, and from 520 to 538 K in Al-2Zn and Al-30Zn alloys, respectively, when the heating rate is increased from 10 to 40 K/min. It is clear for the obtained data that precipitates formed during HPT process drive the transformation rate significantly. As mentioned previously, the low Zn concentration alloys decomposed into GP zones form and/or semi-coherent metastable phase particles, while for high Zn concentration migrating reaction front of two phases is present, leading to the more difficult dissolution process during DSC measurements. This is the reason for the significant shift of about 100 K between the rates of transformation in Al-2Zn and Al-30Zn alloys, at a given heating rate.

Activation energy for dissolution process

As it has already been mentioned, results of the DSC measurements also show that at a given Zn concentration, the peak-temperature of the endothermic peak is shifted to higher temperatures with increasing heating rates [see Fig. 4(b)], indicating that the dissolution is a thermally activated process. In order to determine the activation energy, Q_{ac} characterizing the dissolution process, the generalized Kissinger equation [26]:

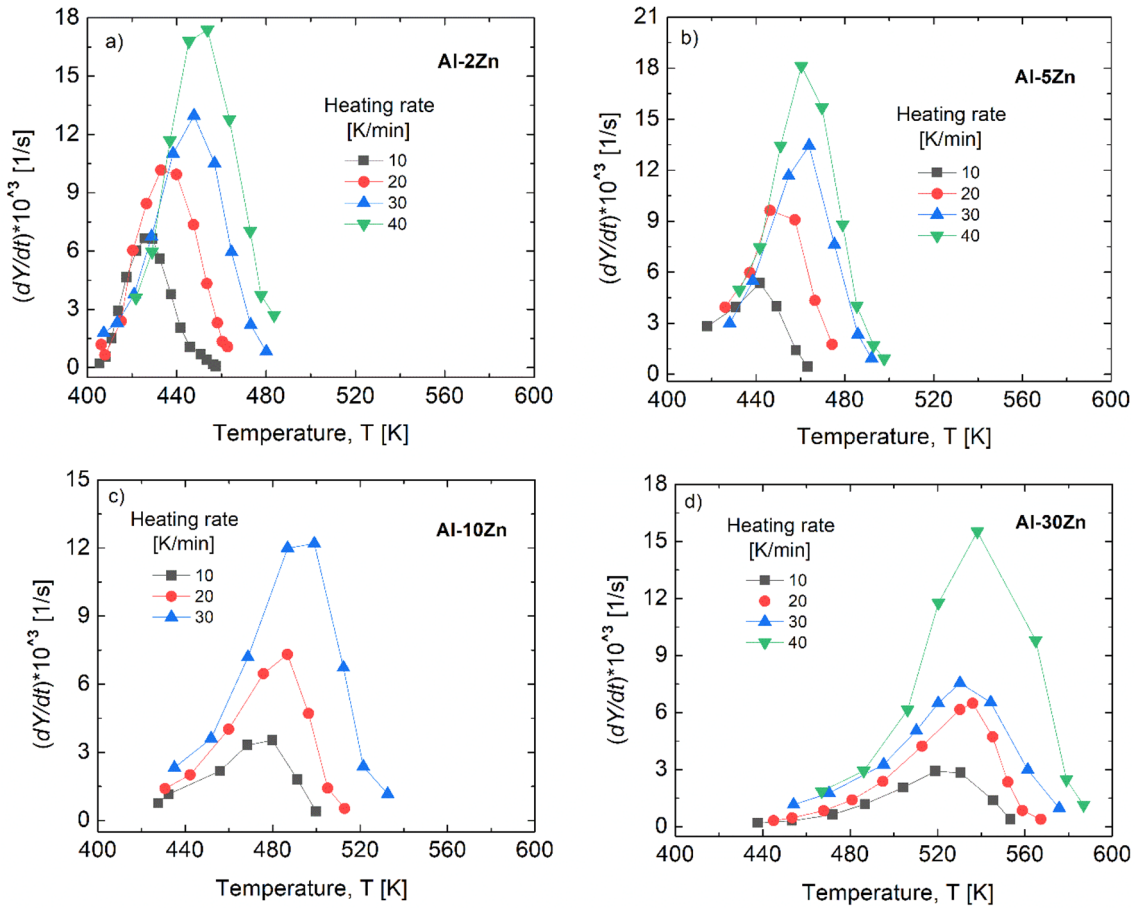


Figure 8: Plots of dY/df - T characterizing dissolutions at different heating rates for (a) Al-2Zn, (b) Al-5Zn, (c) Al-10Zn and (d) Al-30Zn alloys.

$$\ln\left(\frac{V}{T_p^2}\right) = -\frac{Q_{ac}}{RT_p} + C \quad (9)$$

can be used, where V is the heating rate, (in K/min) and T_p is the peak-temperature of the endothermic process for a given Zn concentration, C is a material-constant and R is the universal gas constant.

Figure 9 shows the Kissinger plots obtained for the alloys with different Zn concentrations. It can be seen that for a given Zn concentration, the data points can well be fitted with a linear line. From the slope of this fitted line, according to Eq. (9) the activation energy, Q_{ac} can be determined.

Experimental results show that while the value of the specific enthalpy, ΔH is continuously increasing with the Zn content, the activation energy, Q_{ac} rather characterizes the regions with low and high Zn concentration. In the region of low Zn contents, for Al-2Zn and Al-5Zn alloys, the activation energy is about 88 ± 2.5 kJ/mole, but in the region of higher Zn contents, for the Al-10Zn and Al-30Zn alloys, a much higher value, $Q_{ac} \approx 187 \div 189$ kJ/mole was observed.

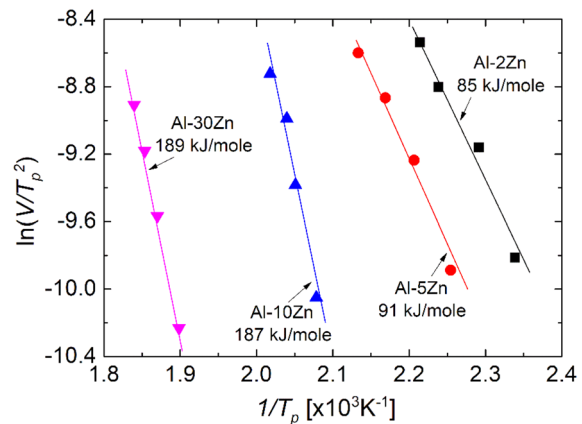


Figure 9: Kissinger plots for the HPT-processed Al-Zn alloys.

In an earlier work on the same alloys [7] it has been observed that in alloys with Zn concentration below about 5% the SPD induced precipitation process results in the formation of fcc α' Zn-rich particles in the grain interiors. In the higher Zn-containing Al-10Zn and Al-30Zn alloys, however, there is a

significant difference. In Al-10Zn and Al-30Zn alloys, besides the fcc α' Zn-rich particles in the grain interiors, large equilibrium hcp Zn particles are being formed in the grain boundaries and especially in GB triple junctions. The linear dependence of ΔH , the heat of dissolution, on the Zn concentration [Fig. 5(b)] suggests, that the heat of dissolution is practically the same for the fcc α' and for the hcp Zn phase. On the other hand, the significant difference in the activation energies in the low and higher concentration alloys, respectively (Fig. 9) indicates that the rate controlling process is strongly different in the dissolution of the α' (fcc) phase from that of the coarse equilibrium Zn (hcp) particles observed only in GBs of the higher concentration alloys. Consequently, the dissolution of the α' particles, formed in the grain interiors is less sensitive on the heating rate (and also for temperature) than the coarse equilibrium hcp Zn particles formed in the GBs and mainly in triple junctions. The activation energy obtained for the Al-2Zn and Al-5Zn alloys is determined by the dissolution of the α' (grain interior) particles, while that of the two higher concentration alloys is mainly by the dissolution of the hcp Zn phase particles in the GBs and triple junctions. The high activation energy (Q_{ac}) characterizing the microstructure of high Zn-containing Al-10Zn and Al-30Zn alloys is certainly the consequence of the strong decomposition during high-pressure torsion (HPT), which leads to the mentioned abnormal softening of these alloys.

Instead of the abnormal softening in high Zn-containing alloys, it has been shown previously that the dislocation density of the HPT-processed Al-Zn samples—due to the pinning effect of the solute atoms and precipitates—is normally changing, i.e. increasing, in the function of the nominal Zn concentration [19].

Considering the normally changing dislocation density and the different UFG microstructures of low- and high-Zn containing Al-Zn alloys, a schematic representation on the microstructure development and decomposition is suggested, as shown in Fig. 10.

Correspondingly, it can be assumed that the microstructure of these alloys has developed during HPT processing in the following steps:

- (I) Along with the initial rapid, local decomposition, the dislocation density increases due to the intensive plastic deformation, as well as the pinning effect of the solute atoms and precipitates.
- (II) This is accompanied by an ultrafine-grained structure. Due to the above-mentioned effect of solute atoms and precipitates, the higher the initial solute concentration, the smaller the average grain-size formed during HPT.
- (III) In the case of low Zn-containing alloys, where the driving force for precipitation is not so high, only α' (grain interior, fcc phase) particles can be formed together with the UFG structure in the final state.

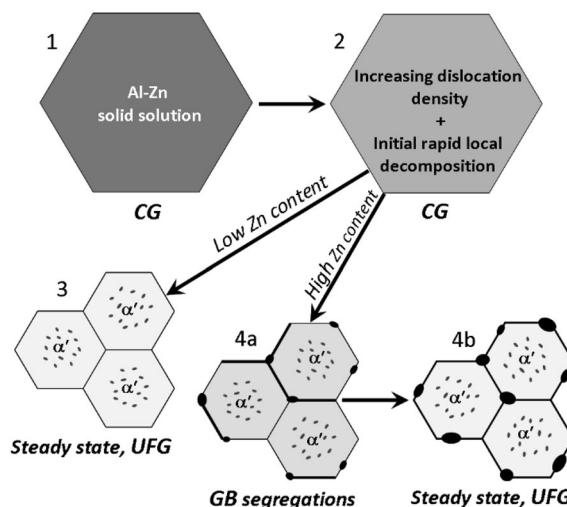


Figure 10: Schematic steps on microstructure-development and decomposition in Al-Zn alloys during the HPT process, representing (1) The initial coarse-grained (CG) solid solution, (2) Early state of plastic deformation, (3) Steady state with UFG structure and α' (fcc) phase particles in low Zn-containing alloys, (4a) Grain boundary segregations in UFG structures of high Zn-containing alloys, and (4b) Steady state with UFG structure containing both α' (fcc) and coarse equilibrium Zn (hcp) phase particles in high Zn-containing alloys.

- (IV) In the case of high Zn-containing alloys, both the high vacancy density and dislocation density formed in the severe plastic deformation promote the uphill diffusion [23]—the segregation of the solute atoms to the grain boundaries, forming Zn particles in the triple junctions and thin Zn-rich layers in boundaries, which are observed with the UFG structure in the final—steady-state.

This assumed scenario may be valid for the similar decomposition observed for other alloys, such as Al-Mg [25, 28], processed also by severe plastic deformation using HPT. Due to the effect of the difference in atomic size, the decomposition is less pronounced for Al-Mg alloys. However, in every case, the severe plastic deformation of supersaturated solid solutions can be considered as a balance of two concurrent processes: the deformation-induced disordering and also deformation-accelerated diffusion, which may result in the grain boundary segregation. Results of this work certainly represent a new strategy to achieve advanced mechanical properties in UFG alloys using grain boundary engineering.

Conclusions

The microstructure and mechanical properties of different concentration HPT-processed, UFG Al-Zn alloys were studied. The main results can be summarized as followings:

- (1) For Zn contents lower than 10 wt%, normal strengthening of ultrafine-grained structure was dominant. For the higher Zn concentrations, despite the Hall–Petch strengthening effect of the fine-grained structure, negative deviation relative to the expected strengthening was observed.
- (2) In alloys having high Zn content, where a significant proportion of the grain boundaries is covered by a Zn-rich layer, results of micro-compression tests have also shown that the room temperature plastic deformation of HPT-processed, high Zn-concentration alloys is characterized by intensive grain boundary sliding and high strain rate sensitivity.
- (3) Results of DSC tests have revealed that the dissolution of the Zn precipitates formed during the HPT process is characterized by a specific enthalpy of dissolution, ΔH and an activation energy, Q_{ac} . While ΔH as expected is increasing with the Zn content, Q_{ac} has strongly different values for the low and high Zn concentrations because of different grain boundary precipitate-structures.
- (4) Based on the experimental observations, a scenario is suggested schematically about that how the decomposed microstructure developed during HPT process in low- and high Zn-containing Al–Zn alloys.

Experimental materials and procedures

High purity (4N) Al and Al–Zn alloys with Zn contents of 2, 5, 10 and 30 wt% were prepared by vacuum induction melting. Disks with diameters of 20 mm and thicknesses of 1.4 mm were solution treated at 500 °C for 1 h, then quenched into room temperature water, providing an annealed (initial) microstructure with an average grain size of about 60–80 μm . The solutionized discs were processed by HPT for 10 revolutions at a rotation speed of 1 rpm under a pressure of 6 GPa. The average grain size of the HPT-processed samples was about 950, 500, 435 and 350 nm for Al-2Zn, Al-5Zn, Al-10Zn and Al-30Zn alloys, respectively [6, 7]. For comparison, the average grain size of ultrafine-grained pure Al is 1200 nm [29].

The microstructure was investigated using a JEOL JEM-2100 transmission electron microscope that operated at 200 kV. For TEM examinations, the disc-shaped samples with a diameter of 3 mm and thickness of 0.1–0.15 mm were twin jet electropolished at temperatures of –25–30 °C and voltages of 10–12 V. Jet polishing of the TEM foils was performed on a Tenupol-5 facility in a solution of 20% nitric acid (HNO_3) and 80% methanol grade B (CH_3OH).

Tensile tests were performed using an INSTRON 5982 universal testing machine with the Bluehill 3 software and a computer system for evaluating mechanical characteristics. Tensile

tests were carried out at strain rates of 10^{-2} , 5×10^{-3} , 10^{-3} , 5×10^{-4} and 10^{-4} s^{-1} at room temperature. The gauge portion of the tensile test samples was $5.7 \times 2 \times 0.6 \text{ mm}^3$. The strain rate sensitivity coefficient values were calculated using the formula:

$$m = \frac{\partial \ln(\sigma)}{\partial \ln(\dot{\epsilon})} \quad (10)$$

where σ is the flow stress, $\dot{\epsilon}$ is the strain rate.

The heat effects accompanying the microstructure changes of the samples were also followed by heating at different heating rates of 10, 20, 30 and 40 K/min in a Perkin-Elmer DSC2 differential scanning calorimeter (DSC) in the temperature range between 300 and 650 K.

Microhardness measurements were performed using a Zwick Roell ZH μ hardness tester with a Vickers indenter at load of 1 N.

Micro-pillars having diameter of $\sim 3 \mu\text{m}$ and height of $\sim 10 \mu\text{m}$ were prepared on the surface of the polished disks using scanning electron microscopy (SEM) and focused ion beam (FIB) functions in a multi-functional Quanta 3D operating at a voltage of 30 kV for different currents of Ga^+ ions. Details on the pillar-preparation are given elsewhere [4].

Micro-compression tests were conducted to deform micro-pillars. The compression measurements were carried out at room temperature using a flat-ended conical diamond indenter at different compressing velocities in a recently developed mobile indentation-unit [30] that can be integrated into the scanning electron microscope for the simultaneous examination of surface morphology.

Author contributions

AQA: formal analysis, investigation, writing—original draft. JL: writing—reviewing, visualization. MYM: investigation, methodology. DU: investigation. EVB: investigation, writing—reviewing. RZV and NQC: conceptualization, methodology, writing—reviewing and editing, supervision.

Funding

Open access funding provided by Eötvös Loránd University. The present research was financed by the Hungarian-Russian bilateral Research program (TÉT) No. 2021–1.2.5-TÉT-IPARI-RU-2021–00001. This work was completed in the ELTE Institutional Excellence Program (TKP2020-IKA-05) financed by the Hungarian Ministry of Human Capacities. R.Z.V., M.Y.M. and E.V.B. acknowledge the support from the Ministry of Science and Higher Education of the Russian Federation under project No. 13.2251.21.0196 (grant agreement No. 075–15–2023–443). The authors thank Dr. Vil U. Kazzykhanov (Ufa University of

Science and Technology) for providing the TEM images presented in Fig. 7.

Data availability

The data that support the findings of this study are all own results of the authors, not available anywhere.

Code availability

Not applicable.

Declarations

Conflict of interest The authors declare that they have no conflict of interest.

Open Access

This article is licensed under a Creative Commons Attribution 4.0 International License, which permits use, sharing, adaptation, distribution and reproduction in any medium or format, as long as you give appropriate credit to the original author(s) and the source, provide a link to the Creative Commons licence, and indicate if changes were made. The images or other third party material in this article are included in the article's Creative Commons licence, unless indicated otherwise in a credit line to the material. If material is not included in the article's Creative Commons licence and your intended use is not permitted by statutory regulation or exceeds the permitted use, you will need to obtain permission directly from the copyright holder. To view a copy of this licence, visit <http://creativecommons.org/licenses/by/4.0/>.

References

- H. Löffler, *Structure and structure development of Al-Zn alloys* (Akademic Verlag, Berlin, 1995)
- G.A. López, E.J. Mittemeijer, B.B. Straumal, Grain boundary wetting by a solid phase, microstructural development in a Zn-5 wt% Al alloy. *Acta Mater.* **52**, 4537 (2004). <https://doi.org/10.1016/j.actamat.2004.06.011>
- R.Z. Valiev, M.Y. Murashkin, A. Kilmametov, B.B. Straumal, N.Q. Chinh, T.G. Langdon, *J. Mater. Sci.* **45**, 4718 (2010). <https://doi.org/10.1007/s10853-010-4588-z>
- N.Q. Chinh, T. Gyóri, R.Z. Valiev, P. Szommer, G. Varga, K. Havancsák, T.G. Langdon, *MRS Commun.* **2**, 75 (2012). <https://doi.org/10.1557/mrc.2012.11>
- N.Q. Chinh, R.Z. Valiev, X. Sauvage, G. Varga, K. Havancsák, M. Kawasaki, B.B. Straumal, T.G. Langdon, *Adv. Eng. Mater.* **16**, 1000 (2014). <https://doi.org/10.1002/adem.201300450>
- E.V. Bobruk, X. Sauvage, N.A. Enikeev, B.B. Straumal, R.Z. Valiev, *Rev. Adv. Mater. Sci.* **43**, 45 (2015)
- X. Sauvage, M.Yu. Murashkin, B.B. Straumal, E.V. Bobruk, R.Z. Valiev, *Adv. Eng. Mater.* **17**, 1821 (2015). <https://doi.org/10.1002/adem.201500151>
- A. Alhamidi, K. Edalati, Z. Horita, S. Hirose, K. Matsuda, D. Terada, *Mater. Sci. Eng. A* **610**, 17 (2014). <https://doi.org/10.1016/j.msea.2014.05.026>
- A.A. Mazilkin, B.B. Straumal, M.V. Borodachenkova, R.Z. Valiev, O.A. Kogtenkova, B. Baretzky, *Mater. Lett.* **84**, 63 (2012). <https://doi.org/10.1016/j.matlet.2012.06.026>
- M.V. Borodachenkova, F. Barlat, W. Wen, A. Bastos, J.J. Gracio, *Int. J. Plasticity* **68**, 150 (2015). <https://doi.org/10.1016/j.ijplas.2014.01.009>
- M. Kawasaki, B. Ahn, P. Kumar, J. Jang, T.G. Langdon, *Adv. Eng. Mater.* **19**, 1600578 (2017). <https://doi.org/10.1002/adem.201600578>
- B.B. Straumal, A.A. Mazilkin, O.A. Kogtenkova, S.G. Protasova, B. Baretzky, *Philos. Mag. Lett.* **87**, 423 (2007). <https://doi.org/10.1080/09500830701225787>
- A.A. Mazilkin, B.B. Straumal, E. Rabkin, B. Baretzky, S. Enders, S.G. Protasova, O.A. Kogtenkova, R.Z. Valiev, *Acta Mater.* **54**, 3933 (2006). <https://doi.org/10.1016/j.actamat.2006.04.025>
- B.B. Straumal, X. Sauvage, B. Baretzky, A.A. Mazilkin, R.Z. Valiev, *Scripta Mater.* **70**, 59 (2014). <https://doi.org/10.1016/j.scriptamat.2013.09.019>
- K. Edalati, Y. Hashiguchi, H. Iwaoka, H. Matsunaga, R.Z. Valiev, Z. Horita, *Mater. Sci. Eng. A* **729**, 340 (2018). <https://doi.org/10.1016/j.msea.2018.05.079>
- K. Edalati, Z. Horita, R.Z. Valiev, *Sci. Rep.* **8**, 6740 (2018)
- Z. Song, R. Niu, X. Cui, E.V. Bobruk, M.Y. Murashkin, N.A. Enikeev, J. Gu, M. Song, V. Bhatia, S.P. Ringer, R.Z. Valiev, X. Liao, *Acta Mater.* **246**, 118671 (2023). <https://doi.org/10.1016/j.actamat.2023.118671>
- R.Z. Valiev, R.K. Islamgaliev, I.V. Alexandrov, *Prog. Mater. Sci.* **45**, 103 (2000). [https://doi.org/10.1016/S0079-6425\(99\)00007-9](https://doi.org/10.1016/S0079-6425(99)00007-9)
- A.P. Zhilyaev, T.G. Langdon, *Prog. Mater. Sci.* **53**, 893 (2008)
- N.Q. Chinh, P. Jenei, J. Gubicza, E.V. Bobruk, R.Z. Valiev, *Mater. Lett.* **186**, 334 (2017). <https://doi.org/10.1016/j.matlet.2016.09.114>
- E.V. Bobruk, X. Sauvage, N.A. Enikeev, R.Z. Valiev, *Mater. Lett.* **254**, 329 (2019). <https://doi.org/10.1016/j.matlet.2019.07.097>
- R.B. Figueiredo, T.G. Langdon, *J. Mater. Res. Technol.* **14**, 137 (2021). <https://doi.org/10.1016/j.jmrt.2021.06.016>
- Z. Kovács, N.Q. Chinh, *Scripta Mater.* **188**, 285 (2020). <https://doi.org/10.1016/j.scriptamat.2020.07.055>
- M.A. Meyers, A. Mishra, D.J. Benson, *JOM* **58**(4), 41 (2006). <https://doi.org/10.1007/s11837-006-0214-6>
- B.B. Straumal, B. Baretzky, A.A. Mazilkin, F. Philipp, O.A. Kogtenkova, M.N. Volkov, R.Z. Valiev, *Acta Mater.* **52**, 4469 (2004). <https://doi.org/10.1016/j.actamat.2004.06.006>
- M.J. Starink, *Int. Mater. Rev.* **49**, 191 (2013). <https://doi.org/10.1179/095066004225010532>
- K.S. Ghosh, N. Gao, *Trans. Nonferrous Met. Soc. China* **21**, 1199 (2011). [https://doi.org/10.1016/S1003-6326\(11\)60843-1](https://doi.org/10.1016/S1003-6326(11)60843-1)

28. Y. Tang, W. Goto, S. Hirosawa, Z. Horita, S. Lee, K. Matsuda, D. Terada, *Acta Mater.* **131**, 57 (2017). <https://doi.org/10.1016/j.actamat.2017.04.002>
29. C. Xu, Z. Horita, T.G. Langdon, *Acta Mater.* **55**, 203 (2007). <https://doi.org/10.1016/j.actamat.2006.07.029>
30. Á.I. Hegyi, P.D. Ispánovity, M. Knappek, D. Tüzes, K. Máthis, F. Chmelik, I. Groma, *Microsc. Microanal.* **23**, 1076 (2017). <https://doi.org/10.1017/S1431927617012594>

Publisher's Note Springer Nature remains neutral with regard to jurisdictional claims in published maps and institutional affiliations.